Amorphizing noble metal chalcogenide catalysts at single-layer limit toward hydrogen production

Yongmin He[1,2,5 *], Liren Liu[3,4], Chao Zhu[2,11], Shasha Guo[2], Prafful Golani[2], Bonhyeong Koo[6], Pengyi Tang[7], Zhiqiang Zhao[4], Mangzhang Xu[2,8], Chao Zhu[2], Peng Yu[9], Xin Zhou[10], Caitian Gao[12], Xuewen Wang[8], Zude Shi[1], Lu Zheng[8], Jiefu Yang[2], Byungha Shin[6], Jordi Arbiol[7,13], Huigao Duan[14], Yonghua Du[15,16], Marc Heggen[17], Rafal E. Dunin-Borkowski[17], Wanlin Guo[4], Qi Jie Wang[5,18*], Zhuhua Zhang[4*], Zheng Liu[2,5,18,19*]

[1]State Key Laboratory of Chemo/Biosensing and Chemometrics, College of Chemistry and Chemical Engineering, Hunan University, Changsha 410082, China.
[2]School of Materials Science and Engineering, Nanyang Technological University, Singapore 639798, Singapore.
[3]Department of Physics, School of Physical and Mathematical Sciences, Nanjing Tech University, Nanjing 210009, China.
[4] State Key Laboratory of Mechanics and Control of Mechanical Structures Key Laboratory for Intelligent Nano Materials and Devices of Ministry of Education, and Institute for Frontier Science, Nanjing University of Aeronautics and Astronautics, Nanjing 210016, China.
[5]Center for Opto-Electronics and Biophotonics, School of Electrical and Electronic Engineering & The Photonics Institute, Nanyang Technological University, Singapore 639798, Singapore.
[6]Deparment of Materials Science and Engineering, Korea Advanced Institute of Science and Technology, Daejeon 34141, Republic of Korea.
[7]Catalan Institute of Nanoscience and Nanotechnology (ICN2), CSIC and BIST, Campus UAB, Bellaterra, Barcelona 08193, Spain.
[8]Institute of Flexible Electronics (IFE), Northwestern Polytechnical University, Xi'an 710072, China.
[9]State Key Laboratory of Optoelectronic Materials and Technologies, School of Materials Science and Engineering, Sun Yat-sen University, Guangzhou 510275, China.
[10]NUS Graduate School, National University of Singapore, 21 Lower Kent Ridge Rd, Singapore 119077
[11]SEU-FEI Nano-Pico Center, Key Lab of MEMS of Ministry of Education, School of Electronic Science and Engineering, Southeast University, Nanjing 210096, China
[12]School of Physics and Electronics, Hunan University, Changsha 410082, China.
[13]ICREA, Pg. Lluís Companys 23, 08010 Barcelona, Catalonia, Spain
[14]College of Mechanical and Vehicle Engineering, Hunan University, Changsha 410082, China.
[15]Institute of Chemical and Engineering Sciences, Agency for Science, Technology and Research, Singapore 627833, Singapore.
[16]National Synchrotron Light Source II, Brookhaven National Laboratory, Upton, NY 11973, USA.
[17]Ernst Ruska-Centre for Microscopy and Spectroscopy with Electrons and Peter Grünberg Institute, Forschungszentrum Jülich GmbH, 52425 Jülich, Germany
[18]CINTRA CNRS/NTU/THALES, UMI 3288, Research Techno Plaza, Singapore, Singapore.
[19]Environmental Chemistry and Materials Centre, Nanyang Environment and Water Research Institute, Nanyang Technological University, 637141, Singapore

Yongmin He, Liren Liu, Chao Zhu, and Shasha Guo contributed equally to this work

*E-mail: ymhe@hnu.edu.cn, qjwang@ntu.edu.sg, chuwazhang@nuaa.edu.cn, and z.liu@ntu.edu.sg

Abstract

Rational design of noble metal catalysts with the potential to leverage efficiency is vital for industrial applications. Such an ultimate atom-utilization efficiency can be achieved when all noble metal atoms exclusively contribute to catalysis. Here, we demonstrate the fabrication of wafer-size amorphous $PtSe_x$ film on SiO_2 substate via a low-temperature amorphizing strategy, which offers single-atom-layer Pt catalysts with high atom-utilization efficiency (~26 wt%). This amorphous $PtSe_x$ ($1.2<x<1.3$) behaves as a fully-activated surface accessible to catalytic reactions, and it is featured by a nearly 100% current density relative to a pure Pt surface and reliable production of sustained high-flux hydrogen over a 2-inch sized wafer as a proof-of-concept. Furthermore, an electrolyser is demonstrated to generate a high current density of 1000 mA cm^{-2}. Such an amorphization strategy is potentially extendable to other noble metals, including Pd, Ir, Os, Rh, and Ru elements, demonstrating the universality of single-atom-layer catalysts.

Introduction

The high cost of noble metal sources, such as platinum and palladium, has hindered the broad deployment of fuel cells and metal-air batteries for commercial applications towards a sustainable energy development.[1-3] Taking the automotive system market as an example, the usage of the total Pt content in fuel cells was about 0.117 g/kW$_{gross}$ in 2018, and it will be cut down to 0.108 g/kW$_{gross}$ in 2020 and as low as 0.064 g/kW$_{gross}$ in 2025 for the cost demand in fuel cell systems.[4] In order to reduce the cost, nanostructuring noble metal in various dimensions presents a promising strategy to improve utilization efficiency and lower the mass loading as well (see Supplementary Table 1)[5,6]. Currently, they have been engineered into 3D porous structures[7,8], 2D nanosheets[9,10], 1D nanowires[11,12], 0D clusters[13] (Figure 1a), or even as small as individual atoms[14-16] (Figure 1b). Such a trend will evolve into an ultimate landscape of the noble metal atoms at the monolayer limit (for thickness ~1 nm), that is, single-atom-layer catalysis (Figure 1c), wherein nearly all the atoms are reconfigurable for a maximum density while being accessible to catalytic reactions, capable of electrocatalytic activities and stable thermodynamically.

In this work, we demonstrate the synthesis of single-atom-layer Pt catalysis, exampled by atom-thin amorphous $PtSe_x$ as a hydrogen evolution reaction (HER) electrocatalyst and its potential to increase the Pt utilization (Figure 1c). First, we report the synthesis of wafer-scale, one-nanometer-thick $PtSe_x$ layer with amorphous yet robust structures through ion etching of pre-deposited 2D $PtSe_2$ under a low-density Ar plasma at a temperature of -30 ^oC. The loss of selenium atoms in the amorphous layer yields a stable Pt single-atom-layer phase on its surface, as evidenced by complementary characterizations, including atomic resolution aberration-corrected (AC) high angle annular dark-field (HAADF) scanning transmission electron microscopy (STEM), Raman spectroscopy, X-ray photoelectron spectroscopy (XPS), and X-ray absorption spectroscopy (XAS), electrical measurements, and supported by intensive first-principles calculations. Next, our micro-

electrochemical cell measurement shows that the amorphous $PtSe_x$ layer exhibits excellent catalytic performance as that of a pure Pt surface with an onset potential of 0 V *vs.* RHE, Tafel slope of 39 mV dec^{-1}, and current density of 25 mA cm^{-2} at a low potential of 50 mV *vs.* RHE. The utility of the wafer-scale amorphous $PtSe_x$ layer is further demonstrated in a water electrolyzer, showing sustainable production of hydrogen. These results open a way to optimize the catalytic performance of 2D and similar materials based on amorphization.

Results

Fabrication of atomically thin amorphous film

We used low-temperature deep reactive ion etching (DRIE) with a low-density Argon (Ar) plasma to convert the atomically-thin crystalline $PtSe_2$ (1T phase) film into an amorphous $PtSe_x$ film. First, a 2-inch wafer-size $PtSe_2$ film was prepared through a two-step selenylation of Pt metal (a ~0.6 nm thickness) on a SiO_2/Si substrate, as explained in Supplementary Figure 1. Then, the as-grown film was etched by DRIE at a low-temperature of -30 ºC for 50 seconds to obtain the amorphous $PtSe_x$ layer ($1.2<x<1.3$). Figure 1d shows a ~1-nm thickness and wafer-scale $PtSe_x$ film on a SiO_2/Si substrate (Supplementary Figure 2). With a wet transfer method (as reported in Supplementary Figure 3), a uniform and continuous film was suspended on a Cu-supported lacey carbon transmission electron microscopy (TEM) grid, as shown in Figure 1e.

In order to characterize the synthesized $PtSe_x$, we conducted atomic-resolution HAADF imaging *via* the STEM (Figures 1f-g and Supplementary Figures 4-5). The dark-field images of the $PtSe_x$ film show a random distribution of the Pt atoms (bright spots in the image) in the film (Figure 1g). Interestingly, there is no long-range order in the atomic arrangement, indicating that the achieved film is amorphous. Moreover, the typical FFT spectrum (a 20×20 nm^2 area) has a broad and continuous halo (Figure 1f) with no diffraction spots, which better visualizes a complete amorphization at an area up to nearly 4000 nm^2 (Supplementary Figure 4). Next, we randomly chose five regions in the $PtSe_x$

film, whose STEM images showed a uniform amorphization process over a large-scale (Supplementary Figure 5). This amorphization process is also verified by Raman spectra, which exhibit nearly negligible characteristic peaks (E_g and A_{1g}) compared to the crystalline $PtSe_2$ film (Figure 1h). Different from previously reported carbon amorphous monolayers[17] (0.6 nm thickness), our amorphous $PtSe_x$ layer is made of Pt and Se atoms with more complicated coordination and, to the best of our knowledge, is the first binary amorphous layer. Notably, our amorphous layer can be thermodynamically stable in a 2D form with a thickness down to 1 nm. Such a highly stable, ultrathin amorphous layer has been long sought, since it can expose nearly all the Pt atoms to electrocatalysis, as will be discussed later.

The formation of the amorphous layer is largely attributed to the low-temperature processing and the low-density Ar plasma. The low-temperature selenization of Pt films avoids the solid-state dewetting behavior[18] to form a porous film (Supplementary Figure 6), and the low-temperature substrate (approximately -30 ºC, during DRIE) suppresses the plasma-induced local heating that may cause aggregation of surface atoms and lead to incomplete amorphization (Supplementary Figure 7). The low-density Ar plasma[19] drives the phase transition of $PtSe_x$ smoothly by adjusting the etching duration. During the DRIE process, the original film evolves from a crystalline 1T phase ($PtSe_2$), via a defected-1T phase and then a mixture of amorphous structure/1T phase ($PtSe_{1.3<x<1.4}$), finally to a completely amorphous structure ($PtSe_{1.2<x<1.3}$), as shown in Supplementary Figure 8.

We further performed XPS and XAS measurements to probe the local electronic structure of Pt atoms in the amorphous $PtSe_x$. The XPS measurement shows that both Pt(IV) and Pt(II) present in Pt 4f region, while no significant Pt(0) peaks are found (Figures 1i and Supplementary Figures 9-10). These XPS data at Pt 4f indicate that the amorphous $PtSe_x$ is a Pt-Se compound but not isolated Pt and Se nanoparticles, consistent with our STEM observations. In XAS measurement, no pronounced Pt-Pt bond peak was found in amorphous $PtSe_x$, confirming no isolated Pt nanoparticles (Supplementary

Figure 11). Compared with crystalline $PtSe_2$, a less Pt-Se coordination number in $PtSe_x$ (N=5.1) and an elongated bond length (~0.02 Å) were observed in XAS data, indicating that the structural homogeneity is reduced in the amorphous structure. Finally, the back-gate electrical measurements (Figure 1j) show that the amorphous $PtSe_x$ exhibits a high conductance (a resistivity of ~0.03 Ω mm) and no gating effect (inset of Figure 1j), in contrast to a p-type semiconducting behavior of crystalline $PtSe_2$. This result suggests an amorphization-induced metallization of the $PtSe_x$ layer.

Formation mechanism of the amorphous film

We then performed *ab initio* calculations to understand the formation mechanism of amorphous $PtSe_x$ (see Methods section). To mimic the loss of Se atoms induced by ion etching, Se atoms were removed sequentially from a perfect single-crystal $PtSe_2$ while ensuring that the removed atom at each step is the one that costs minimum energy. Note that we cannot simulate a real amorphous structure but aim to shed light on the local structural evolution induced by DRIE. To quantify the structural-deformation degree of $PtSe_x$ induced by the Se removal, we define a parameter based on the displacement of Pt atoms, δ_{Pt}, expressed by $\delta_{Pt} = |P_i\text{-}P_i^0|$ with $i = 1, 2, \ldots N$, where N is the total number of Pt atoms in the supercell, P_i and P_i^0 are the positions of i^{th} Pt atom in the $PtSe_x$ and perfect single-crystal $PtSe_2$, respectively. Then, an averaged displacement of Pt is given by $\langle\delta_{Pt}\rangle = \Sigma\,|P_i\text{-}P_i^0|/N$. The sequential Se removal yields a distinct vacancy order in the film, in which each Se vacancy connects to its neighbors with four-coordinated Pt atoms (Figure 2a$_1$). However, the 1T framework of defective $PtSe_x$ is barely distorted even when x decreases to 1.5, as supported by calculated δ_{Pt} and $\langle\delta_{Pt}\rangle$ shown in Figure 2a$_2$. These results suggest that the crystalline structure of $PtSe_x$ (*i.e.,* $1.5<x<2$) is rather robust to short-term ion-etching, in line with our experimental results.

Further decreasing the ratio of Se ($x<1.5$) leads to three-coordinated Pt atoms. Every two of these three-coordinated Pt atoms resulting from the same Se removal, shift towards each other to stabilize the 2D $PtSe_x$ (see circles in Figure 2a$_1$), then severely disturbing the local bond networks. However,

the overall structure remains essentially crystalline if the three-coordinated Pt atoms are insufficiently dense (Figure 2a$_1$). In our calculations, both relaxed structures and calculated $<\delta_{Pt}>$ suggest that the local amorphization starts at a Se/Pt ratio of ~1.38, and a complete amorphization occurs at a ratio of 1.33 with $<\delta_{Pt}>$ exceeding 1.0 Å (Figures 2a and 2b, Supplementary Figures 12-18, and Source Data). The amorphization roots in the randomness of creating three-coordinated Pt atoms across the whole layer. For the amorphous $PtSe_{1.33}$, we already cannot find long-range lattice order within our supercell. The general trend of amorphization agrees with our experimental observation (Supplementary Figure 8). Further decreasing x in 2D $PtSe_x$ enhances the amorphous characteristic, as evidenced by relaxed structures of $PtSe_{1.33}$, $PtSe_{1.30}$, $PtSe_{1.27}$, and $PtSe_{1.25}$ (Figure 2a and 2b).

Experimentally, the detailed amorphous structure is analyzed by mapping the precise position of Pt atoms in $PtSe_x$ based on our STEM imaging (Figure 2c), which allowed us to determine the projected distances between two adjacent Pt atoms onto the basal plane. The data for a perfect $PtSe_2$ sheet is taken as a reference. It turns out that the projected Pt-Pt distances in the amorphous $PtSe_{1.33}$ are peaked at ideal 3.73 Å but exhibit a much broader distribution over 3.0–4.5 Å than those in a perfect $PtSe_2$ (Figure 2d and Supplementary Figure 19). These distances agree well with our *ab initio* molecular dynamical calculations regarding the broad distribution and the peak position (Figure 2d), so do the Pt-Se bond angles in the 2D $PtSe_x$ (Supplementary Figure 20). Such a broad distribution of the bond geometry also echoes the results in the reported amorphous carbon monolayers[17] and O–Si–O bonds in a silica bilayer[20], featuring a 2D amorphous network without long-ranged order.

We also carried out the cross-sectional STEM to investigate the amorphous monolayer's structure (see details in Methods). Figure 2e shows the bright-field (BF, e$_1$) and HAADF (e$_2$) STEM images of the cross-sectional structure, exhibiting the amorphization of the surface $PtSe_x$ monolayer (highlighted by the white dashed lines), in sharp contrast to the well crystalline $PtSe_2$ under layers. The parallel intensity profiles (Figure 2f) show that the amorphous $PtSe_x$ monolayer possesses the inconsistence of

both the intensity distribution and interatomic distance, indicating an obvious in-plane displacement of Pt atoms compared to the periodic profile of crystalline $PtSe_2$ monolayer. The vertical intensity profiles (Figure 2g) exhibit a reduced intensity and broadened peak of amorphous $PtSe_x$ monolayer, verifying an out-of-plane displacement of Pt atoms. These results suggest that the Pt displacement can occur in any direction but is strictly restricted within a single layer, forming amorphous $PtSe_x$ monolayer structure.

Catalytic activity of amorphous film

The hydrogen evolution reaction (HER) activity of the amorphous $PtSe_x$ is tested using micro-electrochemical cells[21,22], as shown in Figure 3a and Supplementary Figures 21-22. Starting from the same mechanically exfoliated $PtSe_2$ nanosheet, we etched different regions at controlled duration and obtained regions of perfect single-crystal, defective single-crystal, and amorphous $PtSe_x$ for a fair comparison among their HER activities. Note that this cell structure can exclude the possible influence raised from underlying $PtSe_2$ (Supplementary Figures 23-24). The electrocatalytic performances of these regions are summarized in Figure 3b and Supplementary Figure 25: First, the basal plane of perfect single-crystal is HER-inert, as has been widely measured[19,23]; Second, at the initial stage of the plasma etching, only isolated Se vacancies are created as active sites, yielding a moderate HER performance (onset potential: ~0.1 V *vs.* RHE and Tafel slope: ~100 mV dec^{-1}). An increased number of Se vacancies results in an enhanced HER performance; Third, as the treatment continues, amorphous $PtSe_x$ is formed and exhibits excellent catalytic performance, *e.g.*, onset potential of 0 V *vs.* RHE, Tafel slope of 39 mV dec^{-1}, and current density of 25 mA cm^{-2} at 50 mV *vs.* RHE for the $PtSe_{1.26}$. A sharply improved performance is observed during this process due to the transition of the catalytic site, that is, from Se vacancies to the amorphous Pt sites.

We next tested tens of micro-devices and combined the calculation of Gibbs free energy of adsorbed hydrogen atoms (ΔG_H) on perfect single-crystal, defective single-crystal, and amorphous

$PtSe_x$ to detailly investigate the transition of active sites (Figure 3c and Supplementary Figure 26). For a pristine crystalline $PtSe_2$, the calculated ΔG_H for inequivalent sites is higher than 1 eV (Figure 3c$_2$), indicating their poor catalytic activity that agrees with our experiments (Figure 3c$_1$). When Se vacancies are introduced in the $PtSe_x$ monolayer, the spectrum of ΔG_H is broadened, and an overall trend is that the values of ΔG_H get closer to zero with increasing the vacancy density (x decreases from 1.8 to 1.5, see Figure 3c$_2$). This is in line with our experimental results, which show that the catalytic performance is enhanced with decreasing x (Figure 3c$_1$). Significant change arises when the $PtSe_x$ monolayer is amorphized upon further decreasing x to 1.4. In this case, active sites are remarkably propagated, as evidenced by the crowding of ΔG_H near-zero eV, due to the existence of three-coordinated Pt structure. This result also agrees with the measured superior catalytic performance of the amorphized $PtSe_{1.26}$.

It is compelling to see that the amorphous $PtSe_x$ offers comparable catalytic performance to pure Pt, which is featured by onset potential: 0V *vs.* RHE, Tafel slope: 37 mV dec^{-1}, and current density: 25 mA cm^{-2} at 50 mV *vs.* RHE (Figures 3b and 3d). The Tafel curves in Figure 3d reveal a similar rate-limiting step for the reaction kinetics between the amorphous $PtSe_x$ and pure Pt[24], rendering the amorphous $PtSe_x$ with a Pt-like catalytic characteristic. More importantly, the nearly 100% current density indicates a maximal density of active sites enabled by the amorphous structure (Figure 3e). This ratio, to the best of our knowledge, is record-high in current TMD catalysts, especially in light of that the current density is less than 1% in PtX_2 (X=S, Se, Te) and other TMDs and ranged between 4-55% in metallic VS_2, VSe_2, NbS_2, $Nb_{1.35}S_2$, and TaS_2 catalysts (see Supplementary Figure 27 and Table 2 for comparison).

To gain further insight into the electrocatalytic performance of amorphous $PtSe_x$, we take the hydrogen coverage into account to evaluate the catalytic activity of the whole layer. This is because the amorphous $PtSe_x$ layer may provide a layer of Pt sites with different reactivities. The hydrogen

coverage[25,26] is defined as $\theta = \frac{N_H}{M_{Pt}} \times 100\%$, where N_H is the number of hydrogen atoms and M_{Pt} is the total number of Pt sites (Supplementary Figures 28-37). The hydrogen coverage varies from 2.8% to 27.8 % (see Supplementary Note 1). Unlike Pt in single-atom catalysts (*e.g.*, Pt-doped in TMDs[27] and graphene[15]), the Pt atoms with diverse bond geometries in the amorphous $PtSe_x$ yield a wide range of ΔG_H shown in Figure 3f. If we consider that ΔG (eV) of the active sites falls in the range of (-0.2, 0.2) (see Supplementary Note 2 and Figure 38), then ~ 25 wt% Pt atoms could contribute to the HER at a hydrogen coverage of 28%. Such an unusual high-density of active sites is attributed to three-coordinated Pt atoms that not only enhance the density of states of 5d orbitals near the Fermi level but also provide a favorable coordination environment for catalysis (Supplementary Figures 39-40). Based on the calculations, we tentatively estimate an atom-utilization efficiency of Pt atoms up to ~25 wt% in the amorphous $PtSe_x$. This value is very close to that obtained from our Cu-underpotential-deposition measurement (~26 wt%, Supplementary Figure 41) and is much higher than ~5 wt% in previously proposed single-atom Pt catalysts[6]. Such a high atom-utilization efficiency may explain why the amorphous $PtSe_x$ can deliver a nearly 100% current density relative to the pure Pt metal. Thus, we coin the amorphous $PtSe_x$ as single-atom-layer catalyst (Figure 3g), a type of Pt catalyst comparable or even superior to the widely studied single-atom or other reported Pt catalysts (see Supplementary Table 3).

Stability and large-scale hydrogen production of amorphous catalyst

As a proof-of-concept for hydrogen generation, the 2-inch amorphous $PtSe_x$ layer is transferred onto an Au substrate for mass production of hydrogen. Figure 4a shows a large amount of hydrogen bubbles produced from this catalyst (also see Supplementary Figure 42 and Supplementary Movie 1). We further examine the catalytic stability of amorphous $PtSe_x$. The chrono-potentiometric test (overpotential versus time) conducted for 100 hours shows that this amorphous $PtSe_x$ also possesses long-term stability at both small and large current densities, *i.e.* 20 and 140 mA cm^{-2}, respectively (Figure 4b and Source Data). What is more, after the long-term testing, its morphology and structures

are well retained, confirming the stable amorphous structure during the HER process (Supplementary Figures 43-44).

We also made a two-electrode electrolyser cell for overall water splitting, as shown in Figure 4c. The assembled full-cell consists of an amorphous $PtSe_x$ layer on a FTO substrate as a cathode and an IrO_x film as an anode (see the inset of Figure 4c and Supplementary Movie 2). The reaction initially has a low onset potential of 1.25 V, close to the theoretical voltage limit (1.23 V). Meanwhile, the current density of this electrolyser is as high as 250 mA cm^{-2} at 1.7 V, and later reaches up to 1000 mA cm^{-2}. These parameters are superior to the reported electrolysers based on thin 2D materials with a current density of 10-100 mA cm^{-2} at similar reaction potentials[28], and are even close to those of industrial Pt and Ir electrolysers (~ 1000 mA cm^{-2})[29,30]. In real applications, the loss or deactivation of noble metal catalysts remains a major issue. To address this issue, we developed a layer-by-layer replenishment method of amorphous $PtSe_x$ using a controlled etching (Supplementary Figures 45-46). Once the old amorphous $PtSe_x$ layer becomes catalytically inactive, a new amorphous layer will be replenished. Such a process persists at least to the sixth new layer without obvious decay in current densities and Tafel slopes, suggesting a successful replenishment.

Figure 5a presents a general approach to achieve amorphous noble MX_x libraries (M=Pt, Pd, Ir, Os, Ru, Rh; X=S, Se) via defect engineering. As the defect concentration increases, the original lattice structure is increasingly distorted. The as-produced amorphous MX_x would be stable in air due to the inert nature of noble metals, as demonstrated by $PtSe_x$ in our work. Indeed, our high-throughput *ab initio* molecular dynamics calculations suggest that all other noble metal selenide layers, such as $PdSe_2$, $IrSe_2$, $OsSe_2$, $RuSe_2$ and $RhSe_2$, form stable amorphous layers as well (Figure 5b, Source Data, and Supplementary Figure 47). Notably, our preliminary experiments have realized a stable amorphous $PdSe_x$ layer (Supplementary Figures 48-49). In contrast, most non-noble metal (Mo, W, Re, etc)-based

MX_x are unstable or even decompose in air due to the corrosion and oxidation of exposed metal atoms (see MoS_2 as an example in Figure 5a and Supplementary Figure 50).

Conclusions

We have demonstrated a highly stable amorphous layer of noble metal chalcogenides, as exemplified by amorphous $PtSe_x$, by Ar-plasma etching of pristine noble metal dichalcogenides at low temperatures, and disclosed the transition mechanism of amorphous $PtSe_x$ from perfect $PtSe_2$. This amorphous $PtSe_x$ layer of ~1 nm thickness provides a robust single-layer of noble metal atoms that exhibits electrocatalytic performance rivaling that of pure noble metals, along with an high atom-utilization efficiency. A two-electrode electrolyser cell made of $PtSe_x$ as cathode and IrO_x as anode has delivered promising overall water splitting performance compared to existing 2D materials-based devices. Beyond the $PtSe_x$ material, our work also opens opportunities to design a family of noble metal single-atom-layer catalysts from their amorphous selenides, such as $PdSe_x$, $IrSe_x$, $OsSe_x$, $RuSe_x$, and $RhSe_x$, boosting great potentials for various electrocatalytic applications.

Methods

Fabrication of water-size $PtSe_x$ film.

There are three steps involved in the fabrication process: First, depositing ~0.6 nm thick Pt layers on a clean 2-inch sapphire or SiO_2/Si wafer by e-beam evaporation at the rate of 0.1 Å s^{-1}. The deposition temperature of the substrate is kept at room temperature to avoid the agglomeration of the film; Second, selenizing those metal films in a CVD apparatus, which is depicted in detail in Supplementary Figure 1. Selenium powder is loaded in an Aluminum Oxide boat and placed both at the upstream and middle of the tube, enabling a continuous supply of Selenium vapor sources. The selenylation temperature was first kept at 200 ºC in low-vacuum conditions at 10-100 kPa for 1-2 hours. This low temperature will avoid the solid-state dewetting behavior[18] to form a porous film (Supplementary Figure 6). Later, it was increased up to 550 ºC to realize the complete selenylation. Third, The samples were finally exposed to an Ar plasma atmosphere at a low temperature (approximately -30 ºC) for various treatment durations. The low-density Ar plasma was generated by a deep reactive ion etching (DRIE) system (Oxford PlasmaLab System 100) with a 5 W RF power in a vacuum chamber (10^{-3} torr of plasma pressure). A low pressure promises a short mean free path for the radicals in a plasma atmosphere. A low-temperature (approximately -30 ºC) substrate will hinder the plasma-induced local heating that usually causes surface atoms' aggregation and leads to an uncompleted amorphization.

First-principles calculations

The calculations were performed within the density functional theory (DFT) framework with the Perdew-Burke-Ernzerh (PBE) functional[31], as implemented in the Vienna Ab initio Simulation Package (VASP) code[32]. A vacuum space of 20 Å was set to eliminate spurious interaction between two $PtSe_x$ surfaces in adjacent periodic images. The core electron-ion interaction was described by the projector augmented wave potential[31,33], and the cutoff energy of the plane-wave basis was set to be 450 eV. We simulated a bilayer $PtSe_2$ with a large 15×15 supercell, where the atoms in the bottom layer were fixed while those in the top layer were allowed to relax. The Brillouin zone integration was sampled using 4×4×1 k-points for the structural optimization, 2×2×1 k-points for *ab initio* molecular dynamics (AIMD) simulations and 16 *k*-points for electronic calculations. The atomic positions were optimized until the maximum force on each atom was less than 0.01 eV/Å. The NVT ensemble was used for AIMD simulations.

The structures of $PtSe_2$ crystal with $PtSe_x$ surface were obtained by sequentially removing Se atoms from the $PtSe_2$ monolayer. Since simple structural optimization was run at zero Kelvin and, thus, tends to reach a local minimum, we performed AIMD calculations for the Se-depleted $PtSe_x$ monolayers to locate the amorphized structures. We raised the simulation temperature to 1000 K to accelerate the structural relaxation for 8 ps. Then, each relaxed structure from the AIMD simulation was fully relaxed at 0 Kelvin. Finally, the thermal stability of all the optimized structures was re-examined by 5 picoseconds AIMD simulation at 800 K. Given the effect of Ar plasma on the $PtSe_x$ surface, the bond rotation in $PtSe_x$ is considered to a certain extent. The atomic coordinates of the optimized models are provided in Source Data.

Theoretical calculation of ΔG_H

The calculations of ΔG_H were also performed by using the PBE-GGA method. A kinetic energy cutoff was set to 500 eV for the plane-wave expansion in this set of calculations. The Gibbs free energies ΔG_H at 300 K were calculated as

$$\Delta G = \Delta E + \Delta E_{ZPE} - T\Delta S_H, \quad (1)$$

$$\Delta E = E_{surf+nH} - E_{surf+(n-1)H} - {}^1/_2\, E_{H_2} \quad n = 1,2,3... \quad (2)$$

$$\Delta E_{ZPE} - T\Delta S_H = 0.173eV, \quad (3)$$

Where T is the temperature, ΔS_H is the entropy of an H atom adsorbed on $PtSe_x$ substrate, $E_{surf+nH}$ is the energy of $PtSe_x$ substrate with n hydrogen atoms and E_{H_2} is the energy of a free H molecule, ΔE_{ZPE} is the zero-point vibrational energy. The harmonic approximation was employed for the vibrational analysis of adsorbates, while gas phase reference molecules are treated as ideal.

Fabrication of $PtSe_2$ nanosheet-based micro-device. First, 16×16 mm SiO_2 (285 nm)/Si chips with pre-patterned 32 Au contact pads were fabricated using photolithography. Second, mechanically-exfoliated $PtSe_2$ nanosheets were transferred onto the chips. Third, the metal electrodes were made on the nanosheet by electron-beam lithography (EBL) followed by thermal or electron-beam evaporation of 5/60 nm Cr/Au. Finally, the device chip was passivated with 500 nm poly(methylmethacrylate) (PMMA) film, followed by an EBL process to create the window on the PMMA to expose the regions (d_1-d_N) of interest on the nanosheet. As the PMMA is inert in the potential range investigated, we expect the electrochemical reactions to only occur on the exposed regions. Note that we choose the mechanically-exfoliated $PtSe_2$ nanosheet due to its perfect atomic surface, guaranteeing that no other activity sites (defects or edges) can interfere with the measurement. The thickness of the employed $PtSe_2$ nanosheet is about 21 nm. The reaction windows were opened at the desired regions on the same nanosheet with various Ar-plasma treatment times. As a result, this micro-cell method allows a rigorous (or even semi-quantitative) investigation on the surface evolutions of $PtSe_2$ from the 1T phase to amorphous. Additionally, the thickness influence of underlying $PtSe_2$ on the HER performance was examined by thicknesses-dependent micro-devices (Supplementary Figure 23) and *in-situ* electronic/electrochemical measurements (Supplementary Figure 24). A negligible effect was observed, indicating a reliable measurement in our cell.

Fabrication of 40 nm-thick Pt film-based micro-device. In order to precisely compare the electrocatalytic performance between Pt and amorphous $PtSe_{1.3}$, we made a Pt microelectrode. A variety of Pt/Ti (40nm/2nm) nanostrips were fabricated onto the aforementioned pre-patterned chip by laser writing method followed by electron-beam evaporation of 2 nm Ti and 40 nm Pt. The bottom Ti layer employed here is served as an adhesion layer between Pt film and SiO_2/Si substrate. Same as the above micro-cell device, a reaction window was opened on PMMA passivation film by EBL to expose Pt film for HER measurement.

Micro-electrochemical measurement

A micro-electrochemical measurement[21,34] was employed in our work. Among the four electrodes, two were connected to graphite (high-purity) and Ag/AgCl micro reference electrode (Harvard Apparatus, see calibration in Supplementary Figure 22) to function as the counter and reference, respectively. The other two electrodes were connected to the $PtSe_x$ nanosheets as drain and source contacts to collect

their conductive and electrocatalytic signals during the HER process. In all experiments, only the exposed region of nanosheets contributes to the electrocatalytic performance, and the rest area in contact with electrolyte was passivated using PMMA film. During a micro-cell measurement, the scan rate of electrochemical potential is 10 mV/step. The electrocatalytic current density was calculated by normalizing the current to the open area of PMMA on the nanosheets. In this work, we express the electrochemical reference voltage with respect to RHE, given by

$$E_{RHE} = E_{Ag/AgCl} + 0.219\ V \quad (4)$$

The mass activity of Pt in our amorphous $PtSe_{1.26}$ catalyst is evaluated using the following equation:

$$Mass\ activity_{Pt} = \frac{I}{m} = \frac{J(mA\ cm^{-2})}{66.2\% \times \rho\ (mg\ cm^{-3}) \times t(cm)} = \frac{J}{0.313}\ A\ mg_{Pt}^{-1}) \quad (5)$$

where J is the current density, ρ is the density of $PtSe_{1.26}$ catalyst (4732.69 Kg/m^3), and t is the thickness of catalyst (~1 nm). The amorphous $PtSe_x$ catalyst gives a Pt mass activity of 16.31 A/mg_{Pt} at 20 mV *vs.* RHE.

Macro-electrochemical measurements

The macro-electrochemical measurements were conducted on a glassy carbon electrode (3 mm in diameter), where the top of the rod (electrode surface) can be screwed off to facilitate the operation. Using a similar PMMA-assist transfer method described above, we transferred an 0.5×0.5 cm^2 amorphous $PtSe_x$ layer made from CVD-grown $PtSe_2$ on a glassy carbon electrode, and the sample area exceeding to glassy carbon electrode was scraped off before measurements (the atom-thin film's mass loading is 0.47 μg cm^{-2}). A standard three-electrode cell was used, where a graphite (high-purity) rod and an Ag/AgCl electrode served as counter and reference electrodes, respectively. The measurements were conducted on a biological electrochemical station in an H_2-saturated 0.5 M H_2SO_4 solution. Linear sweep voltammetry (LSV) was conducted at a scan rate of 5 mV s^{-1}, and the onset potential is defined as the beginning potential of the Tafel linear region. The stability tests were carried out by two methods: continuous potential cycling in the potential window of -0.151 to ~ 0.219 V *vs.* RHE at a scan rate of 100 mV s^{-1}; time-dependent overpotential (η) curve under j = 20 mA cm^{-2} and 140 mA cm^{-2} in 0.5 M H_2SO_4 aqueous solution. The current density was normalized by the geometric surface area of the electrode.

Preparation of IrO_x electrocatalyst: Titanium plate with a size of 2.5 x 2.5 cm^2 was used as a substrate to deposit Ir. Prior to deposition, Ti plate was ultrasonicated with acetone (3 min), isopropyl alcohol (3 min), and DI water (3 min) to remove organic and inorganic contaminants on the surface, followed by N_2 blowing and drying. Then, Ti plate was immediately loaded to the e-beam evaporator with a base pressure of mid-10^{-6} Torr. A 50 nm thick Ti was deposited as an adhesive layer, and a 100 nm thick Ir was deposited with a fixed deposition rate of 1.0 Å/s. After deposition, Ir/Ti plate was connected with Sn-Cu wire, and the edges were sealed by an epoxy (Hysol 9460). And then, Ir/Ti plate was immersed in 1 M KOH solution for 1 hour, followed by continuous oxygen bubble formation by chronoamperometry to change iridium to iridium oxide and/or iridium hydroxide.

Electrochemical full-cell measurement: A two-electrode set-up was used to demonstrate

electrochemical full-cell measurement. A $PtSe_x$ on FTO substrate was used as a working electrode. Prior to measurement, solution-processed SiO_x was deposited on $PtSe_x$/FTO to promote the mechanical adhesion of wet-transferred $PtSe_x$ on FTO. A thin SiO_x with thicknesses of 2, 5, 10 nm was tested on $PtSe_x$/FTO, and 5 nm thickness of SiO_x showed the best current-potential characteristics. Details of preparation can be found in reference[35]. After SiO_x formation, the working electrode was connected with lead wire using Ag paste. The edges were sealed by an epoxy (Hysol 9460) except for an active area. An Ir/Ti electrocatalyst was used as a counter electrode. A working electrolyte was 0.5 M H_2SO_4 for hydrogen evolution and 1 M NaOH for oxygen evolution. An H-cell was used to carry out the full-cell measurement. A 30 ml of aqueous electrolyte was filled in an individual cell, and a bipolar membrane (FuelCellStore) was utilized to separate the catholyte and anolyte. Before measurement, both electrolytes were purged with Ar for 30 min to eliminate unknown gas species. A BiStat (Bio-Logic) was used to measure two-electrode full-cell measurement with the scan rate of 20 mV/s.

Material characterizations

The microstructures and morphologies based on amorphous $PtSe_x$ were characterized by optical microscopy, scanning electron microscopy (SEM, FEI 4200), Raman spectroscopy (WITec alpha300 R), micro-X-ray photoelectron spectroscopy (micro-XPS, KRATOS-AXIS NOVA), X-ray absorption spectroscopy (the Singapore Synchrotron Light Source), and Scanning Transmission Electron Microscopy (STEM, JEOL ARM-200F (S)TEM equipped with CEOS CESCOR aberration corrector). The micro-electrochemical measurements were performed using two source meters (Keithley 2400 and 2450), synchronized by the general-purpose interface bus (GPIB) and the LabView script, allowing simultaneous recording of the electronic and the electrochemical signals.

STEM imaging: The STEM imaging was operated at 80 kV acceleration voltage, and the beam was set up to a convergence semi-angle of 28-33 mrad. High Angle Annular Dark Field (HAADF) imaging with the acquisition semi-angle of 68-280 mrad was employed to produce atomically resolved images whose intensity is approximately proportional to the square of the average atomic number Z of the material under investigation. This chemically-sensitive Z-contrast mode is ideally suited to identify the nature of individual atoms directly. Regarding the cross-sectional STEM characterization, the freshly exfoliated $PtSe_2$ nanosheet was first treated by the DRIE at a ~ 50 s duration to generate an amorphous-monolayer surface. Then, this surface was covered by a MoS_2 flake for the subsequently focused ion beam (FIB) milling process and STEM characterization. All the atomic resolution HAADF STEM images presented here were filtered with a Wiener filter. Raman and XPS measurements were conducted on the mechanically-exfoliated single-layer $PtSe_2$ samples with various plasma treatment times.

XPS measurement and fitting: The Pt-to-Se atomic ratio can be qualitatively determined by XPS measurement, based on the following relationship:

$$\frac{X_{Pt}}{X_{Se}} = \frac{I_{Pt_{4f}}/RSF_{Pt_{4f}}}{I_{Se_{3d}}/RSF_{Se_{3d}}} \quad (6)$$

where I_{Pt4f} and I_{Se3d} are the transmission-function-corrected peak area of the Pt 4f and Se 3d core-level spectra, respectively. The relative sensitivity factor (RSF) values for Pt 4f and Se 3d used in the calculation are 5.575 and 0.853, respectively. The peak areas are calculated by integrating the peaks over the energy range after background subtraction. All core-level spectra against the C1s peak

corresponding to the C-C group (284.8 eV) of adventitious carbon were first calibrated to obtain a precise fitting result. Then, the background-subtracted spectra with peaks were fitted by considering parameter constraints, such as peak width (full-width half-maximum), energy separation, peak area ratio of the spin-orbit components, and the Gaussian-Lorentzian character of the peaks.

Data availability

The data that support the plots within this paper or other findings of this study are available from the corresponding authors on reasonable request, included in the published article and its Supplementary Information. The atomic coordinates of the optimized models and the time-dependent overpotential (η) data are provided in Source Data.

Additional information

Supplementary information is available for this paper at Reprints and permissions information is available at www. nature.com/reprints.

Correspondence and requests for materials should be addressed to Y.H., Q.W., Z.Z., and Z.L.

Publisher's note: Springer Nature remains neutral with regard to jurisdictional claims in published maps and institutional affiliations.

Acknowledgements

This work was supported by the Singapore National Research Foundation Singapore programme (NRF-CRP21-2018-0007, NRF-CRP22-2019-0060, NRF-CRP18-2017-02, and NRF–CRP19–2017–01), Singapore Ministry of Education via AcRF Tier 3 (MOE2018-T3-1-002), AcRF Tier 2 (MOE2017-T2-2-136, MOE2019-T2-2-105, and MOE2018-T2-1-176), and AcRF Tier 1 (RG7/18 and 2019-T1-002-034). It was also supported by the National Key Research and Development Program of China (2019YFA0705400, 2021YFE0194200), the National Natural Science Foundation of China (11772153, 22073048, 21763024, 22175203, 22006023), the Natural Science Foundation of Jiangsu Province (BK20190018), the National Key R&D Program of China (2021YFA1500900), the Fundamental Research Funds for Central Universities (531119200209, NE2018002, NJ2020003), and the High-Performance Computing Center of Nanjing Tech University. ICN2 acknowledges funding from Generalitat de Catalunya 2017SGR327 and the project NANOGEN (PID2020-116093RB-C43), funded by MCIN/ AEI/10.13039/501100011033/. ICN2 is supported by the Severo Ochoa program from Spanish MINECO (Grant No. SEV-2017-0706) and is funded by the CERCA Programme/Generalitat de Catalunya. This work has received funding from the European Union's Horizon 2020 research and innovation programme under grant agreement No 823717-ESTEEM3. We thank Salim Teddy (School of Materials Science and Engineering, Nanyang Technological University, Singapore) for XPS data analysis.

Author Contributions

Z.L. and Y.H. conceived and initiated the project. Z.L. and Z.Z.(Dr.) supervised the project and led the collaboration efforts. Y.H. designed the experiments, synthesized $PtSe_x$ films, and performed micro/macro-electrochemical HER measurement. C.Z., P.T., X.Z, M. H, R. D. B., and J.A. performed the TEM, STEM, and cross-section STEM measurements. Z.Z.(Dr.), L.L., W.G., and Z.Z.(Mr) performed the first-principles calculations of ΔG_H. B.K. and B.S. did the electrolyzer-cell measurements. P.G., S.G., M.X., X.W., L.Z., Z.S., C.G., J.Y., and H.D. assisted the material characterizations, device fabrication, and CVD synthesis. Y.D. conducted XAS measurement. P.Y. helped the synthesis of $PtSe_2$ single crystal by the CVT method. Y.H., L.L., Q.W., Z.Z.(Dr.) and Z.L. wrote the paper. All authors discussed the results and commented on the manuscript.

Competing interests

The authors declare no conflict of interest.

Figure captions

Figure 1. Pt single-atom-layer catalysis exampled by an amorphous $PtSe_x$ layer. **a-c,** Possible structural evolution of Pt catalysts from nanocluster (a) to single-atom (b), and finally to single-atom-layer with high-density active atoms (c). **d,** Photograph of a 2-inch wafer of amorphous $PtSe_x$ film with ~1 nm thickness. **e,** TEM image of a suspended $PtSe_x$ amorphous film, showing its uniform, continuous, and atomically thin structure. **g-f,** Atomic-resolution AC HAADF STEM image of an amorphous $PtSe_x$ film in a large region (g) and the typical Fourier-transform (FFT) spectrum in (f), showing a >90% ratio of amorphous regions in the whole film. **h**, Raman spectra of the amorphous film (below) and 1T phase of $PtSe_2$ crystal (above). **i,** Pt 4f XPS spectra of the amorphous film with fitted curves, showing no significant Pt(0) peaks. **j,** I-V curves of amorphous $PtSe_x$ and few-layer crystalline $PtSe_2$. Inset: A back-gate field-effect transistor measurement indicates the metallic property of the amorphous $PtSe_x$.

Figure 2. Formation mechanism of the 2D amorphous $PtSe_x$. a, *ab initio* molecular dynamics simulations for the structural evolution of $PtSe_x$ with decreasing *x*. **a1**: atomic structures from $PtSe_2$ to $PtSe_x$ (Pt atom in red and Se atom in grey). **a2**: cyan line shows the displacement δ_{Pt} of 36 Pt atoms (denoted by 36 radial grey lines) from their ideal positions in a $PtSe_2$ supercell, while the red line gives the averaged displacement of all Pt atoms in $PtSe_x$, that is, $<\delta_{Pt}>$. The atomic coordinates of the optimized models are provided in Source Data. **b**, Theoretical calculation of $<\delta_{Pt}>$ in the 2D $PtSe_x$ as a function of x. An amorphous characteristic can be observed when *x* decreases to 1.38. **c,** Experimental investigation of the distribution of Pt atoms in an amorphous $PtSe_x$ in False-colored atomic resolution AC HAADF STEM. **d,** Statistical distributions of the distance between two adjacent Pt-Pt atoms in an amorphous $PtSe_x$ and crystalline $PtSe_2$ monolayers from both experiment and theory results. The red curve was collected from the experiment results and the green one from the theoretical calculation. **e**, BF (**e1**) and HAADF (**e2**) STEM image of the cross-sectional structure of an amorphous $PtSe_x$ layer. **f**, Parallel intensity profiles of the amorphous $PtSe_x$ layer and crystalline $PtSe_2$ layer, according to the green and red squares in **e2** (HAADF image), respectively. **g**, Vertical intensity profile of the atom columns across amorphous $PtSe_x$ and crystalline $PtSe_2$ layers, according to the orange square in **e2**.

Figure 3. HER activity of amorphous $PtSe_x$ catalyst by a micro-electrochemical cell. a, Optical images of $PtSe_x$ microelectrodes with reaction windows. (a_1) - (a_4) show four typical reaction windows with different plasma treatment times on a single nanosheet, where spatial control of the electrocatalytic reaction was achieved in different regions by carving windows on a passive PMMA layer. **b,** Polarization curves of the $PtSe_x$ nanosheet with treatment duration from 0 to 60 s, corresponding to *x* varying from 2.0 to 1.11. **c,** Transition of HER catalytic sites of $PtSe_x$ as a function of *x*. **c1** (experiment): Onset potentials and Tafel slopes measured on tens of devices, showing: nearly electrochemically inertness of perfect single-crystal $PtSe_2$, moderate activity of defective single-crystal $PtSe_x$ ($1.5<x<2$), and high activity of amorphous $PtSe_x$ ($x\leq1.4$) with a nearly zero onset potential and a 40 mV dec^{-1} Tafel slope; The error bars represent the range of values for those independent devices. **c2** (theory): Gibbs free energy (ΔG_H) of $PtSe_x$ with different *x* from the calculation. **d**, Comparison of the Tafel slopes between amorphous $PtSe_x$ and Pt film. **e,** Current density ratios of TMD-based catalysts with respect to the Pt catalyst at 50 mV *vs.* RHE. The amorphous $PtSe_x$ shows ~100% current density ratio, and the error bars represent the range of its values in our experiment. The data of other TMD-based catalysts and their corresponding Pt catalysts were collected from the literatures. **f,** Calculated Gibbs free energy (ΔG) for hydrogen adsorption on an amorphous $PtSe_{1.33}$ with the coverage varying from 2.8% to 28%. **g,** Schematic of isomer structures of H atoms adsorbed on the

amorphous $PtSe_x$ surface, demonstrating the amorphous $PtSe_{1.33}$ acting as a single-atom-layer catalyst as a whole. The perfect $PtSe_2$ (inert basal-plane) and defective $PtSe_x$ (scattered Se vacancies as active sites) are shown for comparison.

Figure 4. Wafer-scale fabrication and stability of amorphous $PtSe_x$ catalyst. **a,** 2-inch amorphous $PtSe_x$ film fabricated on an $Au/SiO_2/Si$ substrate for mass production of hydrogen gas. **b,** Time-dependent overpotential (η) curves under j = 20 mA cm^{-2} and 140 mA cm^{-2} in 0.5 M H_2SO_4 aqueous solution. **c,** Volt-ampere curves of overall water splitting in the two-electrode electrolyzer, made of an IrO_x anode and a $PtSe_x$ cathode.

Figure 5. Possible amorphous structures in other noble metal selenides. a, Schematic of structural evolution of perfect single-crystal TMDs, showing that the amorphous structures of noble metal-based MX_x (M: Pt, Pd, Ir, Os, Ru, Rh) are possibly stable in air due to resistance to corrosion and oxidation, in contrast to base metal-based MX_x (M: Mo, W, Re, etc) with over-exposed M atoms readily oxidized in O_2/H_2O atmosphere. The optical images show distinct morphologies of MoS_x and $PtSe_x$ in air for 30 days after Ar plasma treatment, where small droplets exist on plasma-treated regions of MoS_2. **b,** Possible amorphous structures obtained from *ab initio* molecular dynamics simulations for $PtSe_x$, $PdSe_x$, $IrSe_x$, $OsSe_x$, $RuSe_x$ and $RhSe_x$ (where x=1.33, Se atom in grey). The atomic coordinates of the optimized models are provided in Source Data.

References

1 Price pressures on metals. *Nat. Catal.* **2**, 735-735 (2019).

2 Li, C. & Baek, J.-B. Recent Advances in Noble Metal (Pt, Ru, and Ir)-Based Electrocatalysts for Efficient Hydrogen Evolution Reaction. *ACS Omega* **5**, 31-40 (2020).

3 Zhang, Y. *et al.* Recent advances in one-dimensional noble-metal-based catalysts with multiple structures for efficient fuel-cell electrocatalysis. *Coord. Chem. Rev.* **450**, 214244 (2022).

4 James, B. *2018 Cost Projections of PEM Fuel Cell Systems for Automobiles and Medium-Duty Vehicles*, <https://www.energy.gov/sites/prod/files/2018/04/f51/fcto_webinarslides_2018_costs_pem_fc_autos_trucks_042518.pdf> (2018).

5 Liu, M., Zhao, Z., Duan, X. & Huang, Y. Nanoscale Structure Design for High-Performance Pt-Based ORR Catalysts. *Adv. Mater.* **31**, 1802234 (2019).

6 Zhang, L., Doyle-Davis, K. & Sun, X. Pt-Based electrocatalysts with high atom utilization efficiency: from nanostructures to single atoms. *Energy Environ. Sci.* **12**, 492-517 (2019).

7 Xu, Y. & Zhang, B. Recent advances in porous Pt-based nanostructures: synthesis and electrochemical applications. *Chem. Soc. Rev.* **43**, 2439-2450 (2014).

8 Chen, C. *et al.* Highly Crystalline Multimetallic Nanoframes with Three-Dimensional Electrocatalytic Surfaces. *Science* **343**, 1339-1343 (2014).

9 Funatsu, A. *et al.* Synthesis of monolayer platinum nanosheets. *Chem. Commun.* **50**, 8503-8506 (2014).

10 Kijima, T. *et al.* Synthesis of Nanohole-Structured Single-Crystalline Platinum Nanosheets Using Surfactant-Liquid-Crystals and their Electrochemical Characterization. *Adv. Funct. Mater.* **19**, 545-553 (2009).

11 Yin, H. *et al.* Ultrathin platinum nanowires grown on single-layered nickel hydroxide with high hydrogen evolution activity. *Nat. Commun.* **6**, 6430 (2015).

12 Li, M. *et al.* Ultrafine jagged platinum nanowires enable ultrahigh mass activity for the oxygen reduction reaction. *Science* **354**, 1414-1419 (2016).
13 Zhao, M. *et al.* Metal–organic frameworks as selectivity regulators for hydrogenation reactions. *Nature* **539**, 76 (2016).
14 Jiang, K. *et al.* Single platinum atoms embedded in nanoporous cobalt selenide as electrocatalyst for accelerating hydrogen evolution reaction. *Nat. Commun.* **10**, 1743 (2019).
15 Cheng, N. *et al.* Platinum single-atom and cluster catalysis of the hydrogen evolution reaction. *Nat. Commun.* **7**, 13638 (2016).
16 Jiang, K. *et al.* Rational strain engineering of single-atom ruthenium on nanoporous MoS_2 for highly efficient hydrogen evolution. *Nat. Commun.* **12**, 1687 (2021).
17 Toh, C.-T. *et al.* Synthesis and properties of free-standing monolayer amorphous carbon. *Nature* **577**, 199-203 (2020).
18 Lee, S.-H., Kwak, E.-H. & Jeong, G.-H. Dewetting behavior of electron-beam-deposited Au thin films on various substrates: graphenes, quartz, and SiO_2 wafers. *Appl. Phys. A* **118**, 389-396 (2015).
19 Li, H. *et al.* Activating and optimizing MoS_2 basal planes for hydrogen evolution through the formation of strained sulphur vacancies. *Nat. Mater.* **15**, 48-53 (2016).
20 Lichtenstein, L. *et al.* The Atomic Structure of a Metal-Supported Vitreous Thin Silica Film. *Angew. Chem. Int. Ed.* **51**, 404-407 (2012).
21 He, Y. *et al.* Self-gating in semiconductor electrocatalysis. *Nat. Mater.* **18**, 1098-1104 (2019).
22 He, Y. *et al.* Engineering grain boundaries at the 2D limit for the hydrogen evolution reaction. *Nat. Commun.* **11**, 57 (2020).
23 Jaramillo, T. F. *et al.* Identification of active edge sites for electrochemical H_2 evolution from MoS_2 nanocatalysts. *Science* **317**, 100-102 (2007).
24 Li, Y. *et al.* MoS_2 nanoparticles grown on graphene: an advanced catalyst for the hydrogen evolution reaction. *J. Am. Chem. Soc.* **133**, 7296-7299 (2011).
25 Wang, T. *et al.* High Coverage CO Activation Mechanisms on Fe(100) from Computations. *J. Phys. Chem. C* **118**, 1095-1101 (2014).
26 Digne, M., Sautet, P., Raybaud, P., Euzen, P. & Toulhoat, H. Use of DFT to achieve a rational understanding of acid–basic properties of γ-alumina surfaces. *J. Catal.* **226**, 54-68 (2004).
27 Li, H. *et al.* Synergetic interaction between neighbouring platinum monomers in CO_2 hydrogenation. *Nat. Nanotechnol.* **13**, 411-417 (2018).
28 Han, N. *et al.* Nitrogen-doped tungsten carbide nanoarray as an efficient bifunctional electrocatalyst for water splitting in acid. *Nat. Commun.* **9**, 924 (2018).
29 Zhigang, S., Baolian, Y. & Ming, H. Bifunctional electrodes with a thin catalyst layer for `unitized' proton exchange membrane regenerative fuel cell. *J. Power Sources* **79**, 82-85 (1999).
30 Altmann, S., Kaz, T. & Friedrich, K. A. Bifunctional electrodes for unitised regenerative fuel cells. *Electrochim. Acta* **56**, 4287-4293 (2011).
31 Perdew, J. P., Burke, K. & Ernzerhof, M. Generalized Gradient Approximation Made Simple. *Phys. Rev. Lett.* **78**, 1396-1396 (1997).
32 Hafner, J. Ab-initio simulations of materials using VASP: Density-functional theory and beyond. *J. Comput. Chem.* **29**, 2044-2078 (2008).
33 Kresse, G. & Joubert, D. From ultrasoft pseudopotentials to the projector augmented-wave method. *Phys. Rev. B* **59**, 1758-1775 (1999).

34 He, Q. *et al.* In Situ Probing Molecular Intercalation in Two-Dimensional Layered Semiconductors. *Nano Lett.* (2019).

35 Labrador, N. Y. *et al.* Enhanced Performance of Si MIS Photocathodes Containing Oxide-Coated Nanoparticle Electrocatalysts. *Nano Lett.* **16**, 6452-6459 (2016).

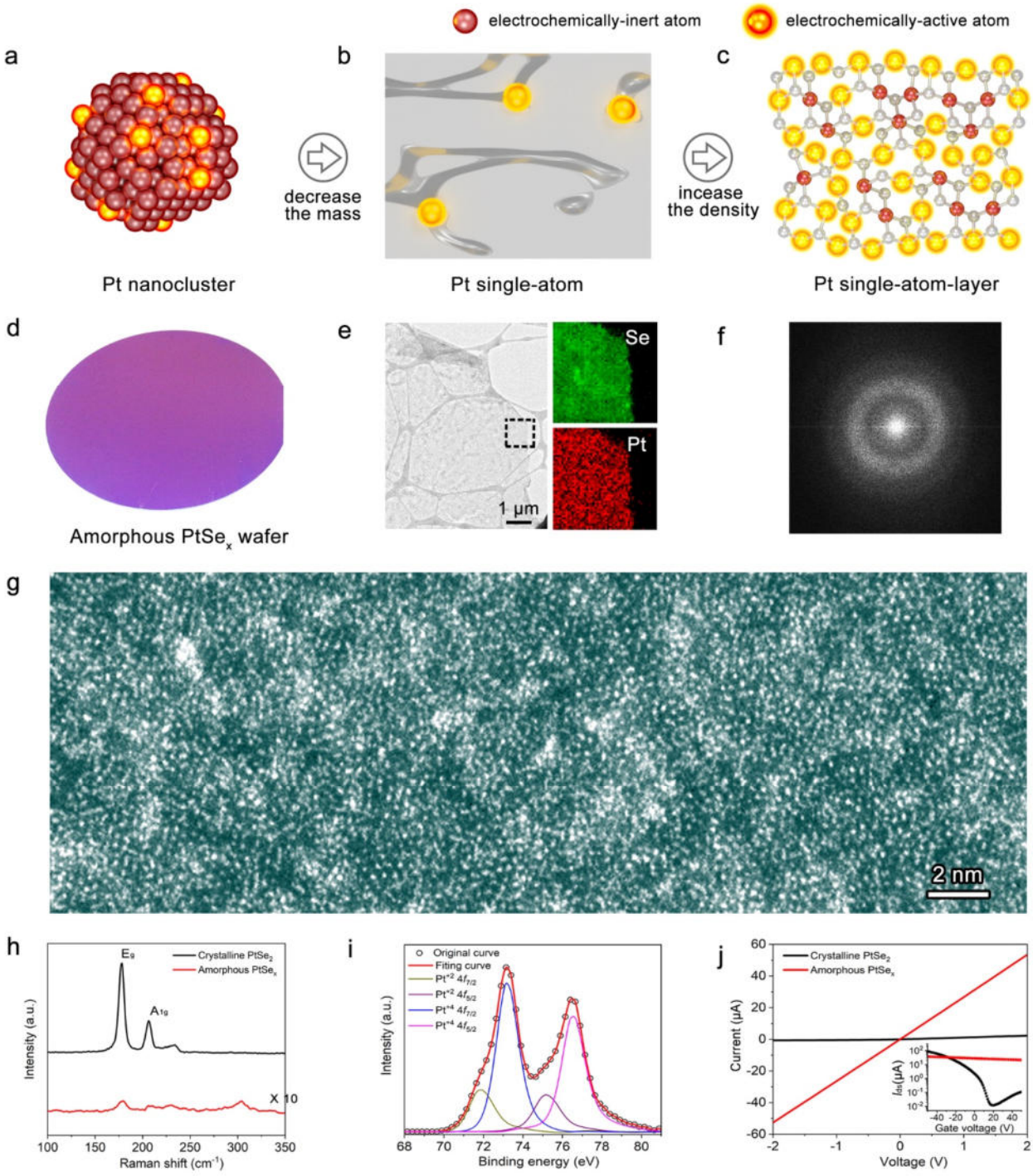

Figure 1. Pt single-atom-layer catalysis exampled by an amorphous PtSe$_x$ layer. **a-c,** Possible structural evolution of Pt catalysts from nanocluster (a) to single-atom (b), and finally to single-atom-layer with high-density active atoms (c). **d,** Photograph of a 2-inch wafer of amorphous PtSe$_x$ film with ~1 nm thickness. **e,** TEM image of a suspended PtSe$_x$ amorphous film, showing its uniform, continuous, and atomically thin structure. **g-f,** Atomic-resolution AC HAADF STEM image of an amorphous PtSe$_x$ film in a large region (g) and the typical Fourier-transform (FFT) spectrum in (f), showing a >90% ratio of amorphous regions in the whole film. **h**, Raman spectra of the amorphous film (below) and 1T phase of $PtSe_2$ crystal (above). **i,** Pt 4f XPS spectra of the amorphous film with fitted curves, showing no significant Pt(0) peaks. **j,** I-V curves of amorphous PtSe$_x$ and few-layer

crystalline $PtSe_2$. Inset: A back-gate field-effect transistor measurement indicates the metallic property of the amorphous $PtSe_x$.

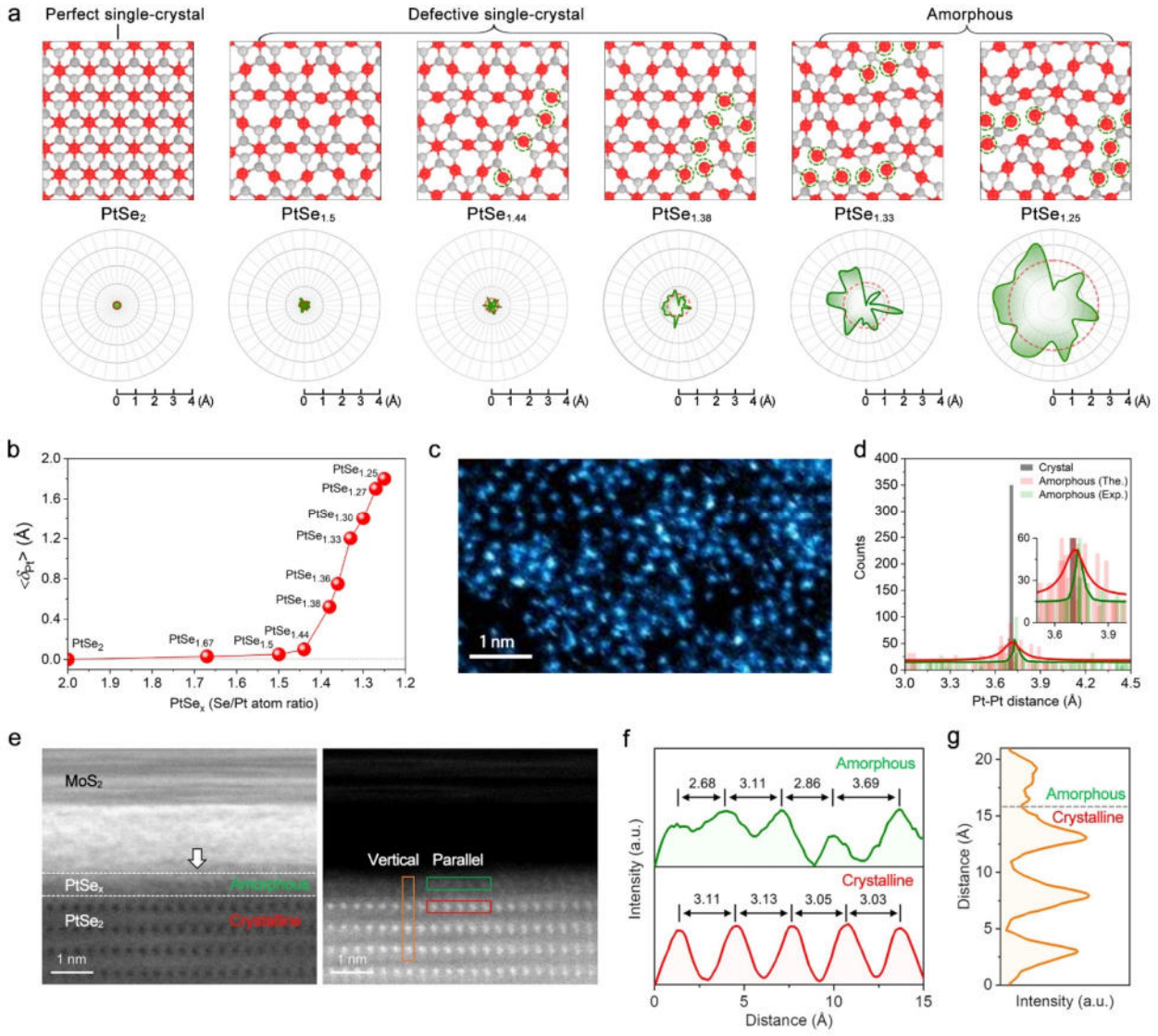

Figure 2. Formation mechanism of the 2D amorphous $PtSe_x$. a, *ab initio* molecular dynamics simulations for the structural evolution of $PtSe_x$ with decreasing *x*. Top panel: atomic structures from $PtSe_2$ to $PtSe_x$ (Pt atom in red and Se atom in grey). Bottom panel: cyan line shows the displacement δ_{Pt} of 36 Pt atoms (denoted by 36 radial grey lines) from their ideal positions in a $PtSe_2$ supercell, while the red line gives the averaged displacement of all Pt atoms in $PtSe_x$, that is, $<\delta_{Pt}>$. **b**, Theoretical calculation of $<\delta_{Pt}>$ in the 2D $PtSe_x$ as a function of x. An amorphous characteristic can be observed when *x* decreases to 1.38. **c,** Experimental investigation of the distribution of Pt atoms in an amorphous $PtSe_x$ in False-colored atomic resolution AC HAADF STEM. **d,** Statistical distributions of the distance between two adjacent Pt-Pt atoms in an amorphous $PtSe_x$ and crystalline $PtSe_2$ monolayers from both experiment and theory results. The red curve was collected from the experiment results and the green one from the theoretical calculation. **e**, BF (left) and HAADF (right) STEM image of the cross-sectional structure of an amorphous $PtSe_x$ layer. **f**, Parallel intensity profiles of the amorphous $PtSe_x$ layer (upper) and crystalline $PtSe_2$ layer (bottom), according to the green and red squares in **e** (right: HAADF image), respectively. **g**, Vertical intensity profile of the atom columns across amorphous $PtSe_x$ and crystalline $PtSe_2$ layers, according to the orange square in **e** (right: HAADF image).

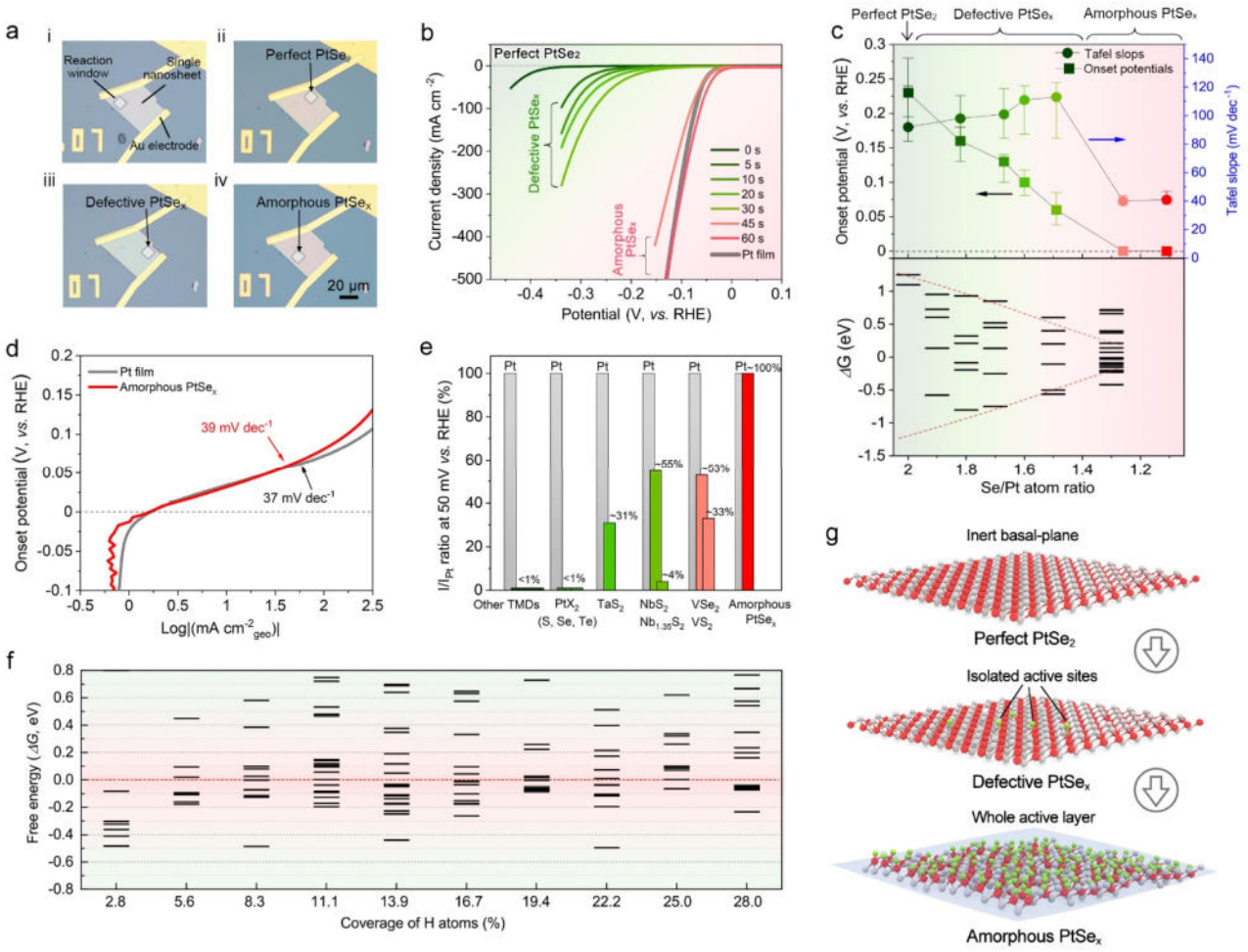

Figure 3. HER activity of amorphous $PtSe_x$ catalyst by a micro-electrochemical cell. a, Optical images of $PtSe_x$ microelectrodes with reaction windows. (i)-(iv) show four typical reaction windows with different plasma treatment times on a single nanosheet, where spatial control of the electrocatalytic reaction was achieved in different regions by carving windows on a passive PMMA layer. **b,** Polarization curves of the $PtSe_x$ nanosheet with treatment duration from 0 to 60 s, corresponding to *x* varying from 2.0 to 1.11. **c,** Transition of HER catalytic sites of $PtSe_x$ as a function of *x*. Top (experiment): Onset potentials and Tafel slopes measured on tens of devices, showing: (i) nearly electrochemically inertness of perfect single-crystal $PtSe_2$, (ii) moderate activity of defective single-crystal $PtSe_x$ ($1.5<x<2$), and (iii) high activity of amorphous $PtSe_x$ ($x\leq1.4$) with a nearly zero onset potential and a 40 mV dec^{-1} Tafel slope; Bottom (theory): Gibbs free energy (ΔG_H) of $PtSe_x$ with different *x* from the calculation. **d**, Comparison of the Tafel slopes between amorphous $PtSe_x$ and Pt film. **e,** Current density ratios of TMD-based catalysts with respect to the Pt catalyst at 50 mV *vs.* RHE; the amorphous $PtSe_x$ shows ~100% current density ratio. The data of each Pt catalyst was collected from the same literature. **f,** Calculated Gibbs free energy (ΔG) for hydrogen adsorption on an amorphous $PtSe_{1.33}$ with the coverage varying from 2.8% to 28%. **g,** Schematic of isomer structures of H atoms adsorbed on the amorphous $PtSe_x$ surface, demonstrating the amorphous $PtSe_{1.33}$ acting as a single-atom-layer catalyst as a whole. The perfect $PtSe_2$ (inert basal-plane) and defective $PtSe_x$ (scattered Se vacancies as active sites) are shown for comparison.

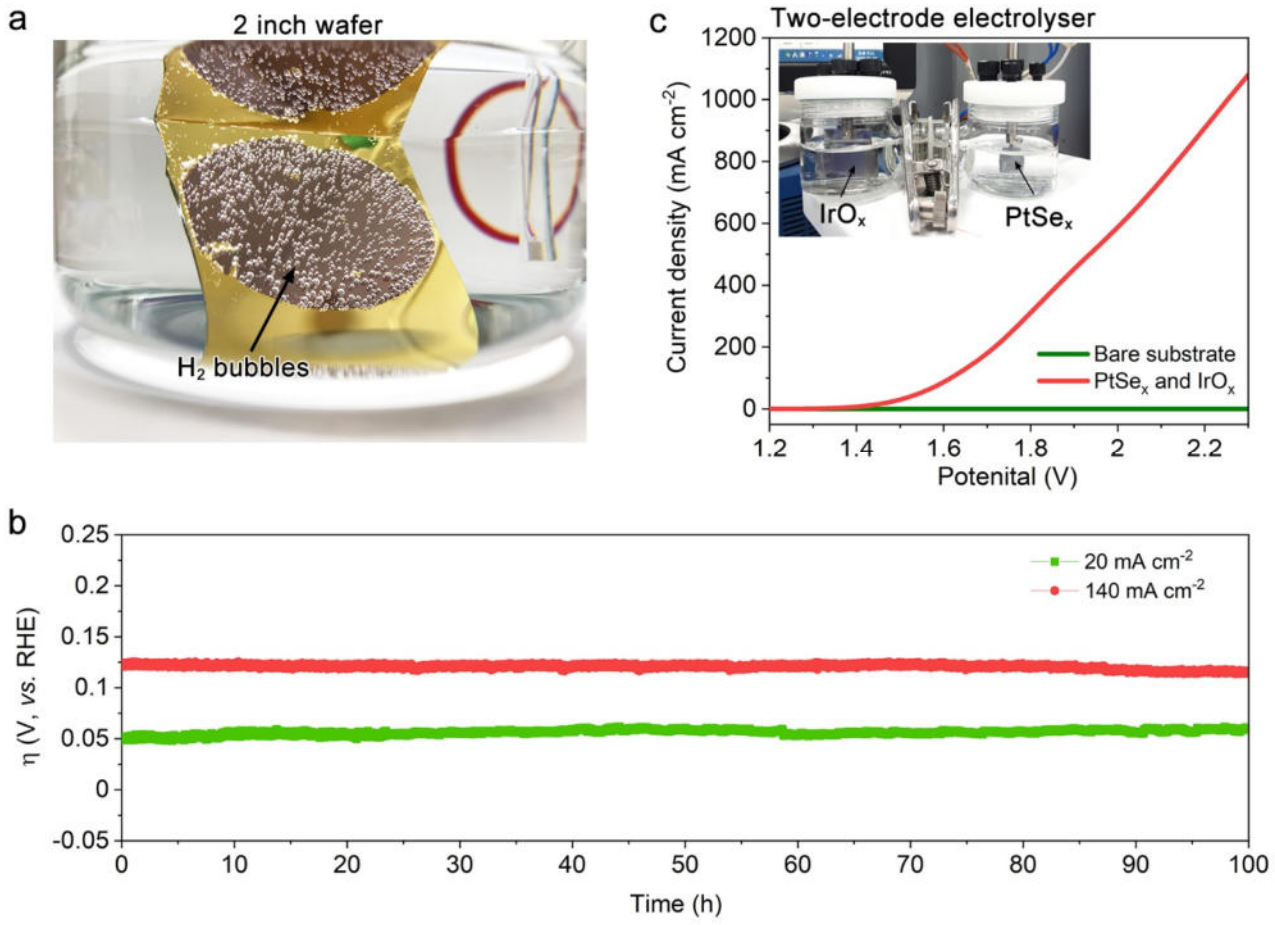

Figure 4. Wafer-scale fabrication and stability of amorphous $PtSe_x$ catalyst. **a,** 2-inch amorphous $PtSe_x$ film fabricated on an $Au/SiO_2/Si$ substrate for mass production of hydrogen gas. **b,** Time-dependent overpotential (η) curves under j = 20 mA cm^{-2} and 140 mA cm^{-2} in 0.5 M H_2SO_4 aqueous solution. **c,** Volt-ampere curves of overall water splitting in the two-electrode electrolyzer, made of an IrO_x anode and a $PtSe_x$ cathode.

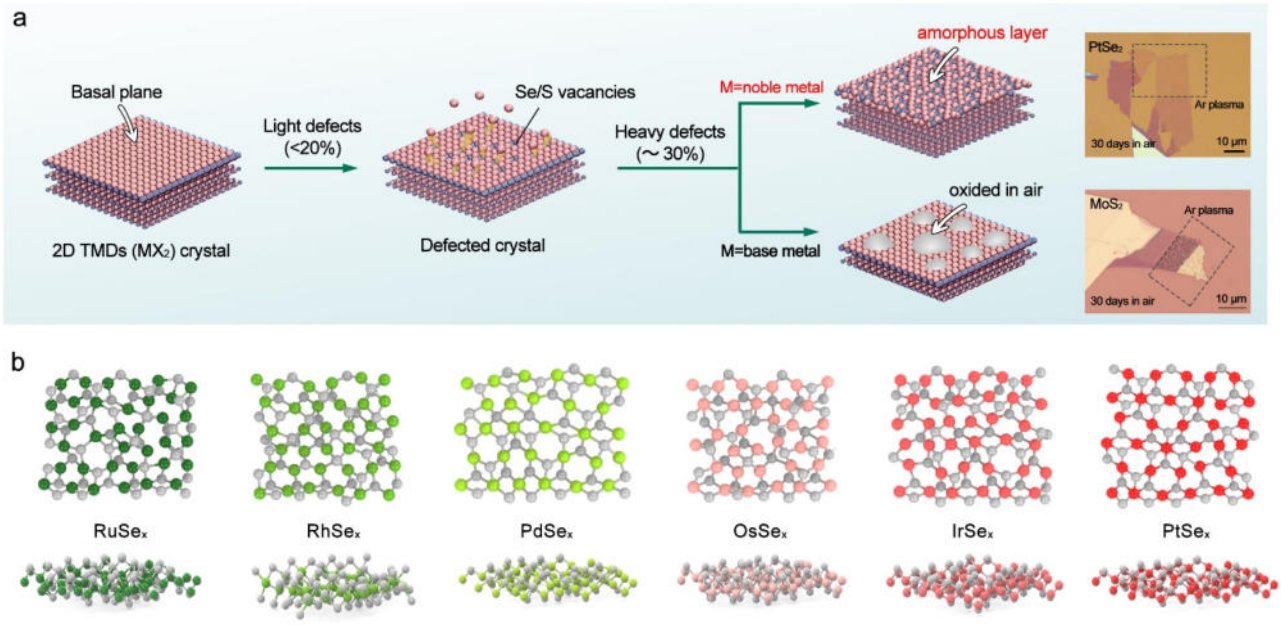

Figure 5. Possible amorphous structures in other noble metal selenides. a, Schematic of structural evolution of perfect single-crystal TMDs, showing that the amorphous structures of noble metal-based MX_x (M: Pt, Pd, Ir, Os, Ru, Rh) are possibly stable in air due to resistance to corrosion and oxidation, in contrast to base metal-based MX_x (M: Mo, W, Re, etc) with over-exposed M atoms readily oxidized in O_2/H_2O atmosphere. The optical images show distinct morphologies of MoS_x and $PtSe_x$ in air for 30 days after Ar plasma treatment, where small droplets exist on plasma-treated regions of MoS_2. **b,** Possible amorphous structures obtained from *ab initio* molecular dynamics simulations for $PtSe_x$, $PdSe_x$, $IrSe_x$, $OsSe_x$, $RuSe_x$ and $RhSe_x$ (where x=1.33, Se atom in grey).